Eng. Sci., 2026, **39**, 1921

Engineered Science
DOI: https://dx.doi.org/10.30919/es1921

Accurate Long-Term Atmospheric Corrosion Prediction of Weathering Steel via SHapley Additive exPlanations (SHAP) Enhanced Neural Network

Yan Bai,[1,2] Baosheng Liu,[1,2,*] Yuezhong Zhang,[1,2] Shaohua Zhang,[1,2] Pengpeng Wu,[1,2] Xiaoxia Ren[1,2,*] and Yinghui Wei[3,*]

Abstract

The growth of the photovoltaic (PV) industry is driving demand for structural materials with superior corrosion resistance, strength, and environmental adaptability. Weathering steels have emerged as promising candidates. However, the long-term atmospheric corrosion performance of weathering steels in complex environments remains insufficiently studied. This paper proposes a data-driven framework to predict corrosion rates of weathering steels based on a neural network model enhanced by SHapley Additive exPlanations (SHAP). The model takes alloy composition, environmental parameters, and exposure time as inputs and outputs the predicted atmospheric corrosion rates. Bayesian optimization is utilized to explore the optimal network configuration and hyperparameter set. SHapley Additive exPlanations is used to identify physically meaningful features, leading to the construction of a SHapley Additive exPlanations -enhanced neural network (ENN). The ENN is evaluated through five-fold cross-validation to assess its robustness and generalization capability, achieving a coefficient of determination (R^2) of 0.941. Furthermore, when tested on one-year independent data, the model maintains a low relative error of 2.31%. Moreover, the predicted long-term corrosion trends of WP720 weathering steel under ISO-defined atmospheric conditions align well with established corrosion mechanisms. These results demonstrate the enhanced neural network reliability, high accuracy, and potential for practical deployment in corrosion forecasting and lifespan assessment of weathering steels.

Keywords: Weathering steel; Atmospheric corrosion; Machine learning; SHapley Additive exPlanations (SHAP).
Received: 16 August 2025; Revised: 26 November 2025; Accepted: 04 December 2025
Article type: Research article.

1. Introduction

In response to the accelerating global transition toward renewable energy, the photovoltaic (PV) industry has witnessed rapid and sustained growth in recent years.[1] This growth has been underpinned by persistent policy support, continuous technological innovation, and steadily declining system costs, leading to a consistent increase in global PV installation capacity.[2] As the scale of PV deployment continues to rise, so does the demand for high-performance structural materials that can ensure long-term system stability under complex and harsh environmental conditions. In this context, structural supports serve as the primary load-bearing component and play a crucial role in maintaining mechanical integrity, resisting corrosion, and adapting to diverse service environments.[3] Their reliability directly impacts the safety, operational efficiency, and service life of PV systems.[4]

Currently, hot-dip galvanized steel and Zn-Al-Mg coated steel are widely used in PV support structures due to their extensive industrial adoption and proven performance in general service conditions.[5] However, in complex environments such as industrial zones, humid climates, and marine atmospheres, these materials are susceptible to accelerated corrosion, which leads to rising maintenance demands, reduced service life, and compromised structural reliability.[6,7] In addition, conventional anti-corrosion treatments often discharge large amounts of heavy metals and acidic or alkaline waste, posing serious environmental risks

---

[1] *College of Materials Science and Engineering, Taiyuan University of Science and Technology, Taiyuan, Shanxi, 030024, China*
[2] *State Key Laboratory of Advanced Stainless Steel, Taiyuan University of Science and Technology, Taiyuan, Shanxi, 030024, China*

and conflicting with global sustainability goals.[8,9] These challenges have prompted increasing interest in developing alternative structural materials that combine high corrosion resistance with low environmental impact.

Weathering steel has emerged as a promising candidate for PV support structures due to its superior mechanical strength and its ability to form a stable, protective rust layer that significantly slows down long-term corrosion processes.[10,11] Nevertheless, conventional weathering steels often suffer from rapid initial corrosion, poor rust layer adhesion, and inadequate stability when exposed to fluctuating environmental factors such as humidity, temperature, and atmospheric pollutants.[12-14] To address these issues, a new generation of super weathering steel WP720 has been developed through optimized alloy composition, offering enhanced strength, stiffness, and reduced weight. However, despite its promising application potential, systematic and quantitative evaluations of WP720's long-term atmospheric corrosion behavior under complex service conditions remain limited.[15] This highlights the urgent need for scientific, data-driven methodologies to assess the durability and service performance of advanced weathering steels such as WP720.

Traditionally, the long-term atmospheric corrosion behavior of weathering steels has been estimated using empirical models, laboratory-based accelerated corrosion tests, or mechanistic models derived under simplified assumptions. While these approaches have contributed to understanding basic corrosion trends, they often fall short in capturing the complex, nonlinear interactions among environmental variables, alloy composition, and exposure time. Moreover, empirical models typically rely on site-specific calibration and lack generalizability, while accelerated tests may not fully replicate field conditions, leading to limited predictive accuracy.[16-18] In this context, machine learning (ML) has emerged as a powerful tool for modeling high-dimensional, nonlinear systems by learning patterns directly from experimental data. By integrating diverse influencing factors, ML-based models offer enhanced predictive accuracy, adaptability to various environments, and potential for long-term corrosion forecasting of advanced weathering steels.[19-22]

Recent advances in ML have demonstrated its effectiveness in modeling complex, high-dimensional systems, offering a promising alternative to conventional corrosion prediction methods. In the field of materials degradation, ML has been increasingly applied to predict corrosion rates of carbon steels, stainless steels, and coated metals under various atmospheric and marine environments, leveraging data from laboratory tests and field exposures. Widely used algorithms, including linear regression models, ensemble methods, kernel-based approaches, and neural networks, have shown strong capabilities in capturing nonlinear relationships among material composition, environmental factors, and exposure time.[23-25]

Despite these advances, the application of ML to weathering steels remains relatively underexplored. In particular, few studies have focused on the coupled effects of alloy composition, climatic parameters, and service time on the long-term corrosion behavior of weathering steels.[26] Most existing ML-based corrosion studies have focused on conventional structural materials, such as carbon and low-alloy steels. These studies are often confined to marine and industrial atmospheres, whereas investigations of weathering steels across diverse atmospheric conditions remain scarce.[27-29] This gap is especially critical given that these factors often interact in complex and nonlinear ways under real-world service conditions. As such, there is a pressing need to develop robust, data-driven frameworks that can accurately assess and predict the durability of weathering steels based on multiple interacting variables.

To address the current limitations in predicting the long-term atmospheric corrosion behavior of weathering steels, this study develops a data-driven modeling framework that incorporates key variables such as alloy composition, environmental parameters, and exposure time. A systematic benchmarking of multiple machine learning algorithms is conducted to evaluate their predictive capabilities. Building upon the best-performing neural network, SHapley Additive exPlanations (SHAP)-based feature selection strategy is employed to enhance the reliability of variable selection and improve overall model performance.[30] Additionally, a log-transformed exposure time feature and a dual-stage validation process are incorporated to better capture nonlinear corrosion trends and further improve model robustness. The SHAP-enhanced neural network (ENN) model not only improves prediction accuracy under complex service conditions but also enhances the robustness and applicability of the corrosion forecasting framework in engineering practice.

2. Experimental methods

2.1 Data collection

This paper compiles corrosion data from three different sources: (1) 13 types of weathering steels tested across six atmospheric test sites in China;[31] (2) 14 types of weathering steels evaluated at two test sites in Spain;[32] (3) corrosion data collected independently by the author in Taiyuan, China. In total, this process yielded 373 valid data points. Each dataset entry comprises chemical compositions of weathering steels, environmental factors, exposure time, and corrosion rate as the target variable. A comprehensive list of input features and their corresponding ranges is summarized in Table 1.

Chemical composition significantly affects the corrosion resistance of weathering steel. To effectively capture this, 14 chemical elements (C, S, P, Mn, Si, Cr, Ni, Mo, Cu, Nb, V, Ti, Al, RE) were selected as descriptors for characterizing 28

---

[3]School of Materials Science and Engineering, Taiyuan University of Technology, Taiyuan, Shanxi, 030024, China
[*]Email: liubaosheng@tyust.edu.cn (B. Liu),
renxiaoxia@tyust.edu.cn (X. Ren),
weiyinghui@tyut.edu.cn (Y. Wei)

Table 1: List of features in the corrosion dataset.

Descriptor	Description	Data range
Material	C content	0.070wt%-0.186wt%
	S content	0.002wt%-0.225wt%
	P content	0.010wt%-0.110wt%
	Mn content	0.300wt%-1.500wt%
	Si content	0.128wt%-0.750wt%
	Cr content	0.000wt%-1.000wt%
	Ni content	0.000wt%-2.920wt%
	Mo content	0.000wt%-0.100wt%
	Cu content	0.000wt%-1.060wt%
	Nb content	0.000wt%-0.050wt%
	V content	0.000wt%-0.050wt%
	Ti content	0.000wt%-0.086wt%
	Al content	0.000wt%-0.045wt%
	RE content	0.000wt%-0.027wt%
Environment	temperature (T)	12.0 °C-24.5 °C
	Relative humidity (RH)	57 %-86 %
	Time of wetness (TOW)	2358 $h\cdot a^{-1}$-6314 $h\cdot a^{-1}$
	Cl^- deposition rate	0.006 $mg\cdot dm^{-2}\cdot d^{-1}$-0.71 $mg\cdot dm^{-2}\cdot d^{-1}$
	SO_2 deposition rate	0.0066 $mg\cdot dm^{-2}\cdot d^{-1}$-0.704 $mg\cdot dm^{-2}\cdot d^{-1}$
Exposure time	Exposure time	0.25 a-16 a
Target property	Corrosion rate	1.5μm/a–596μm/a

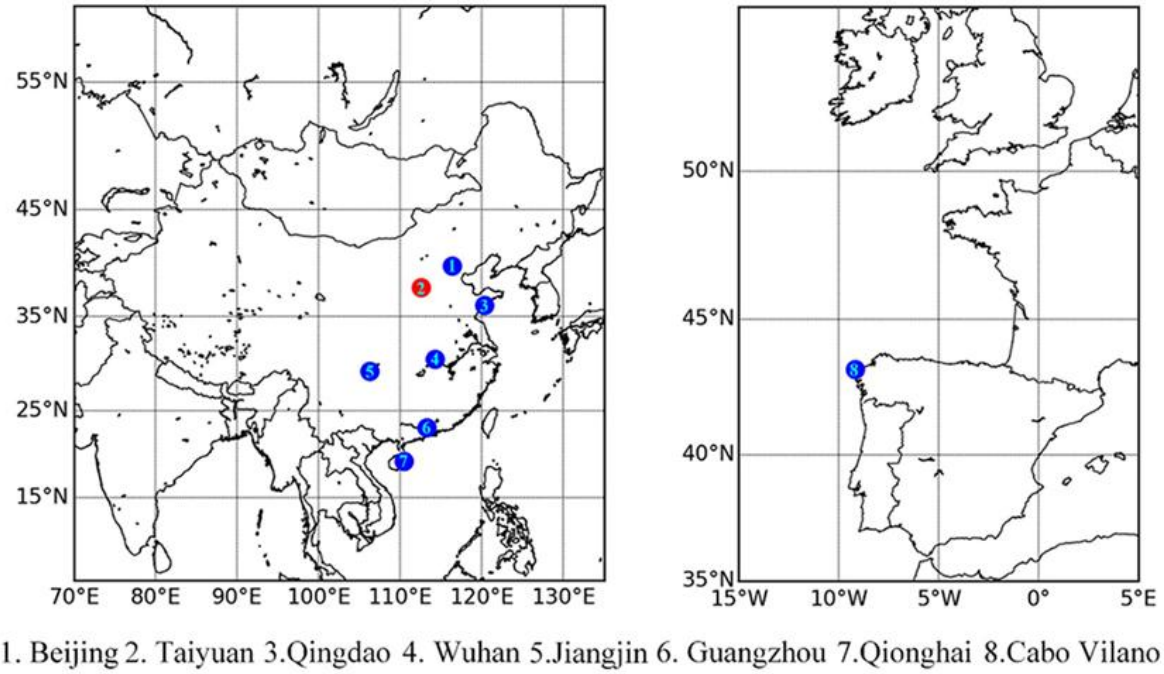

Fig. 1: Distribution of exposure sites for atmospheric corrosion testing.

Table 2: Element compositions of weathering steel in the collected datasets.

Steel	C	S	P	Mn	Si	Cr	Ni	Mo	Cu	Nb	V	Ti	Al	RE
06CuPCrNiMo	0.070	0.023	0.090	0.400	0.500	0.400	0.600	0.000	0.380	0.000	0.000	0.000	0.000	0.000
10CrCuSiV	0.100	0.002	0.010	0.300	0.600	0.800	0.000	0.100	0.250	0.000	0.050	0.000	0.000	0.000
09CuPCrNi	0.110	0.019	0.080	0.400	0.300	0.000	0.400	0.000	0.270	0.000	0.000	0.000	0.000	0.000
09CuPCrNiA	0.080	0.023	0.070	0.400	0.500	0.600	0.300	0.000	0.410	0.000	0.000	0.000	0.000	0.000
09CuPTiRE	0.080	0.019	0.089	0.400	0.300	0.000	0.000	0.000	0.290	0.000	0.000	0.010	0.000	0.010
12CrMnCu	0.130	0.022	0.011	0.800	0.300	0.600	0.000	0.000	0.200	0.000	0.000	0.000	0.000	0.000
09MnNb(s)	0.100	0.024	0.027	1.200	0.200	0.000	0.000	0.000	0.000	0.030	0.030	0.000	0.000	0.000
JN255	0.113	0.023	0.025	0.579	0.164	0.000	0.000	0.000	0.173	0.000	0.000	0.000	0.000	0.000
JN255(RE)	0.114	0.026	0.041	0.475	0.128	0.000	0.000	0.000	0.172	0.000	0.000	0.000	0.000	0.027
JN345	0.137	0.025	0.041	1.220	0.335	0.000	0.000	0.000	0.167	0.000	0.000	0.000	0.000	0.000
JN345(RE)	0.132	0.225	0.034	1.315	0.345	0.000	0.000	0.000	0.154	0.000	0.000	0.000	0.000	0.026
Q450NQR1	0.120	0.008	0.025	1.500	0.750	1.000	0.000	0.000	0.500	0.000	0.000	0.000	0.000	0.000
CortenA	0.120	0.050	0.110	0.350	0.500	0.800	0.650	0.000	0.400	0.000	0.000	0.000	0.000	0.000
C1	0.180	0.013	0.016	0.690	0.290	0.080	0.120	0.000	0.290	0.000	0.000	0.000	0.017	0.000
C2	0.143	0.014	0.027	0.770	0.370	0.090	0.110	0.000	0.570	0.000	0.000	0.000	0.015	0.000
C3	0.186	0.013	0.033	0.680	0.290	0.080	0.120	0.000	1.060	0.000	0.000	0.000	0.019	0.000
C4	0.170	0.011	0.012	0.660	0.250	0.070	0.920	0.000	0.270	0.000	0.000	0.000	0.017	0.000
C5	0.170	0.014	0.011	0.680	0.240	0.070	1.690	0.000	0.270	0.000	0.000	0.000	0.012	0.000
C6	0.175	0.016	0.010	0.700	0.260	0.080	2.830	0.000	0.280	0.000	0.000	0.000	0.010	0.000
C7	0.156	0.011	0.013	0.650	0.260	0.500	0.120	0.000	0.260	0.000	0.000	0.000	0.013	0.000
C8	0.139	0.015	0.019	0.790	0.270	0.085	1.000	0.000	0.520	0.000	0.000	0.000	0.011	0.000
C9	0.154	0.012	0.012	0.690	0.270	0.050	2.250	0.000	0.590	0.000	0.000	0.000	0.014	0.000
C10	0.178	0.015	0.014	0.700	0.250	0.070	2.920	0.000	0.540	0.000	0.000	0.000	0.011	0.000
C11	0.172	0.016	0.019	0.690	0.260	0.540	0.110	0.000	0.540	0.000	0.000	0.000	0.010	0.000
C12	0.151	0.012	0.014	0.680	0.250	0.530	1.000	0.000	0.540	0.000	0.000	0.000	0.010	0.000
C13	0.175	0.015	0.016	0.690	0.250	0.490	1.680	0.000	0.520	0.000	0.000	0.000	0.010	0.000
C14	0.158	0.014	0.011	0.680	0.240	0.460	2.380	0.000	0.500	0.000	0.000	0.000	0.010	0.000
WP720	0.070	0.004	0.013	1.201	0.392	0.719	0.202	0.000	0.292	0.050	0.007	0.086	0.045	0.000

types of weathering steel. Specific elemental compositions for each steel type are detailed in Table 2.

The atmospheric test sites include six locations in China representing different typical climates (Beijing, Wuhan, Guangzhou, Qingdao, Jiangjin, and Qionghai), two test sites in Spain (Cabo Vilano 1 and Cabo Vilano 2), and the experimental site of this paper in Taiyuan, China, as shown in Fig. 1.

In this paper, five key environmental factors were selected due to their significant influence on corrosion: average relative humidity (RH), average temperature (T), time of wetness (TOW), sulfur dioxide concentration (SO_2), and chloride concentration (Cl^-).[33-35] Detailed information on these environmental factors is provided in Table 3.

Table 4 summarizes the exposure times for each weathering steel type. At test sites in China, 13 weathering steel types were exposed for 0.25–16 a. At test sites in Spain, 14 types were exposed for 1–3 a. At the Taiyuan site, WP720 was exposed for 0.25–1 a.

2.2 Data preprocessing

To ensure data quality, reduce noise interference, and improve the predictive performance of the ML model, a systematic data preprocessing procedure was implemented before model training. This procedure consisted primarily of outlier detection, missing value handling, and feature normalization.

Table 3: Environmental characteristics of the atmospheric test sites.

Sites	RH/%	T/°C	TOW/($h\cdot a^{-1}$)	SO$_2$/($mg\cdot dm^{-2}\cdot d^{-1}$)	Cl$^-$/($mg\cdot dm^{-2}\cdot d^{-1}$)
Beijing	57	12	2358	0.442	0.049
Qingdao	71	12.5	4049	0.704	0.25
Wuhan	77	16.82	4871	0.272	0.011
Jiangjin	81	18.4	5304	0.667	0.006
Guangzhou	78	22.4	5048	0.107	0.024
Qionghai	86	24.5	6314	0.15	0.199
Cabo Vilano 1	76	14.4	3504	0.0066	0.2
Cabo Vilano 2	76	14.3	3504	0.0092	0.71
Taiyuan	66	20.8	3102	0.458	0.039

Table 4: Exposure time of weathering steels at different test sites.

weathering steel type	Test sites	Exposure time (a)
06CuPCrNiMo	Beijing Qingdao Wuhan Jiangjin Guangzhou Qionghai	1, 2, 4, 8, 16
10CrCuSiV		1, 2, 4, 8, 16
09CuPCrNi		1, 2, 4, 8, 16
09CuPCrNiA		1, 2, 4, 8, 16
09CuPTiRE		1, 2, 4, 8, 16
12CrMnCu		1, 2, 4, 8, 16
09MnNb(s)		1, 2, 4, 8, 16
JN255		1, 2, 4, 8, 16
JN255(RE)		1, 2, 4, 8, 16
JN345		1, 2, 4, 8, 16
JN345(RE)		1, 2, 4, 8, 16
Q450NQR1		1, 2, 4, 8, 16
CortenA		0.25, 0.5, 1, 2, 3
C1	Cabo Vilano 1 Cabo Vilano 2	1, 2, 3
C2		1, 2, 3
C3		1, 2, 3
C4		1, 2, 3
C5		1, 2, 3
C6		1, 2, 3
C7		1, 2, 3
C8		1, 2, 3
C9		1, 2, 3
C10		1, 2, 3
C11		1, 2, 3
C12		1, 2, 3
C13		1, 2, 3
C14		1, 2, 3
WP720	Taiyuan	0.25, 0.5, 1

Given the presence of extreme environmental conditions, measurement errors, and human-induced variability, the corrosion rate data may contain outliers and missing values. To address these issues, a two-stage outlier detection strategy was adopted. Initially, threshold-based screening was conducted based on prior literature and empirical knowledge to define plausible corrosion rate ranges under different climatic conditions and exposure times. Data points deviating significantly from physically reasonable limits were flagged for further inspection.

In addition to manual screening, a statistical approach based on the interquartile range (IQR) was employed for automatic outlier detection.[36] The IQR and its associated bounds were computed as shown in Eqs. (1)-(3):

$$IQR = Q_3 - Q_1 \tag{1}$$

$$Lower\ Bound = Q_1 - 1.5 \times IQR \tag{2}$$

$$Upper\ Bound = Q_3 + 1.5 \times IQR \tag{3}$$

where Q_1 and Q_3 represent the 25th and 75th percentiles, respectively. Data points falling outside these bounds were identified as statistical outliers.

Considering the high precision requirements of corrosion rate modeling,[37] both outliers and missing values were directly removed rather than subjected to imputation or interpolation, to maintain the integrity and reliability of the dataset.

Since the dataset comprises features with varying units and numerical scales, normalization and transformation techniques were applied to ensure uniformity across variables. Min–max normalization was employed for features such as relative RH%, T/°C, and Exposure time (a), rescaling them to the interval [0,1], as shown in Eq. (4):

$$x_{norm} = \frac{x - x_{min}}{x_{max} - x_{min}} \tag{4}$$

where x_{min} and x_{max} denote the minimum and maximum values of the feature, respectively.

Furthermore, unit-based normalization was applied to the TOW/(h·a⁻¹) to preserve its physical interpretability. Given that corrosion depth typically exhibits a logarithmic growth trend over time, a natural logarithmic transformation was applied to the exposure time to improve linearity and modeling performance, as shown in Eq. (5):

$$\mathrm{X}' = \mathrm{I}n(1 + X) \tag{5}$$

The dataset encompasses various weathering steels, test sites, and exposure times, which may introduce imbalance during the train–test process. To address this, we applied data transformation and normalization, along with five-fold cross-validation for training and evaluation. These measures effectively mitigate the adverse effects of data imbalance and enhance the predictive model's robustness and generalizability.

2.3 Corrosion rate

Weathering steel specimens with dimensions of 50 mm × 20 mm × 2 mm were selected to measure atmospheric corrosion rates using the gravimetric method, based on data from Taiyuan City. All specimens were sourced from the same batch of material. Each specimen was lightly ground using 400-grit sandpaper to remove oxide scale and visible impurities.[38,39] Each specimen was then first treated with anhydrous ethanol to remove oil residues and other organic contaminants, followed by a thorough rinse with deionized water. After drying, the specimens were weighed to determine their initial mass, ensuring uniform surface conditions across all samples. The pretreated specimens were then exposed to open-air conditions in Taiyuan, Shanxi Province (112°E, 38°N), and were retrieved after exposure periods of 90, 180, and 360 days. At each retrieval, three sets of parallel samples were collected, and each set underwent three independent mass measurements to reduce errors caused by environmental fluctuations and manual handling.

After collecting, the specimens underwent mild chemical cleaning to remove corrosion products and residual oxide films. First, they were immersed in anhydrous ethanol to dissolve organic residues, then rinsed thoroughly with deionized water, dried, and reweighed. The mass loss was converted into a corrosion rate in micrometers per annum (μm/a), as shown in Eq. (6):

$$CR = \frac{m_0 - m_1}{\rho \times A \times t} \times 10^4 \tag{6}$$

where m_0 and m_1 are the initial and final masses of the specimen, measured in grams. The parameter ρ denotes the density of the steel in grams per cubic centimeter, A is the effective exposed surface area in square centimeters, and t is the exposure duration, expressed in years and denoted by a.

2.4 Model training and hyperparameter optimization

The dataset comprising 373 samples was partitioned into two subsets: 80% for training and 20% for validation. This partitioning strategy ensures that the validation subset provides an unbiased assessment of model generalization during training, independent of hyperparameter tuning.[40]

To effectively evaluate model performance and mitigate the risk of overfitting, five-fold cross-validation was conducted on the training set. The data were partitioned into five equal subsets, with each subset used once as the validation fold while the remaining four served as the training data. The average validation performance across the five iterations was used to assess the model's robustness and generalization capability.

Hyperparameter optimization was systematically integrated within the cross-validation framework to further enhance the predictive capabilities of the selected ML models.[41] Given the variability in hyperparameter space dimensionality among different models, optimization approaches were carefully selected based on computational feasibility and optimization efficiency. For models characterized by relatively simple, low-dimensional hyperparameter spaces, Grid Search was employed to exhaustively evaluate all predefined hyperparameter combinations. Specifically, the optimal hyperparameter set was identified by minimizing the average validation loss across all cross-validation folds, as shown in Eq. (7):

$$\lambda^* = \arg\min_{\lambda \in \Lambda} \frac{1}{K} \sum_{k=1}^{K} \mathcal{L}\left(f_\lambda\left(X^{(k)}\right), Y^{(k)}\right) \tag{7}$$

where K denotes the number of cross-validation folds, $X^{(k)}$ and $Y^{(k)}$ represent the training and validation subsets in the k-th fold respectively, $\left(f_\lambda\left(X^{(k)}\right)\right.$ denotes model predictions under the hyperparameter set λ and $\mathcal{L}()$ is the loss function employed.

For models with complex, high-dimensional hyperparameter spaces, Bayesian Optimization was adopted due to its computational efficiency and effectiveness in high-dimensional parameter searches. Unlike exhaustive Grid

Search, Bayesian Optimization constructs a probabilistic surrogate model $g(\lambda)$ to approximate the relationship between hyperparameters and model performance. It sequentially selects hyperparameters by optimizing an acquisition function $\mathcal{A}(\lambda|\mathcal{D}_t)$, as shown in Eq. (8):

$$\lambda^* = \arg\max_{\lambda} \mathcal{A}(\lambda|\mathcal{D}_t) \tag{8}$$

where $\mathcal{D}_t$ denotes previously evaluated hyperparameter-performance pairs. In this paper, Expected Improvement (EI) was employed as the acquisition function due to its balanced exploration-exploitation strategy, as shown in Eq. (9):

$$EI(\lambda) = \mathbb{E}[\max(0, f_{best} - g(\lambda))] \tag{9}$$

where f_{best} represents the current optimal observed validation performance, and $g(\lambda)$ denotes the surrogate model's prediction for validation loss. Bayesian Optimization iteratively refines hyperparameter selection, efficiently identifying optimal parameter sets while significantly reducing computational overhead compared to exhaustive methods.

2.5 Evaluation metrics

In this paper, the Mean Squared Error (MSE), Mean Absolute Error (MAE), and Coefficient of Determination (R²) were selected as evaluation metrics to comprehensively assess the predictive performance of the models.[42] These metrics quantify model accuracy and reliability by measuring the deviations between predicted and actual corrosion rates. The mathematical definitions are provided as shown in Eqs. (10)-(12):

$$MSE = \frac{1}{n}\sum_{i=1}^{n}(y_i - \hat{y}_i)^2 \tag{10}$$

$$MAE = \frac{1}{n}\sum_{i=1}^{n}|y_i - \hat{y}_i| \tag{11}$$

$$R^2 = 1 - \frac{\sum_{i=1}^{n}(y_i - \hat{y}_i)^2}{\sum_{i=1}^{n}(y_i - \bar{y})^2} \tag{12}$$

where y_i and $\hat{y}_i$ represent the actual and predicted values for the i-th sample, respectively; n is the total number of samples; and $\bar{y}$ denotes the mean of all actual values.

Specifically, MSE measures the average squared difference between predicted and actual values, heavily penalizing larger errors and thus effectively highlighting model sensitivity to outliers. Lower values of MSE indicate higher prediction precision and consistency. In contrast, MAE provides a more intuitive metric by averaging the absolute deviations, assigning equal weight to all errors. MAE is less sensitive to extreme values compared to MSE, providing a robust evaluation of overall model accuracy. Additionally, the R² evaluates the proportion of variance in the observed data explained by model predictions, typically ranging from negative infinity to 1. Higher values closer to 1 indicate better predictive performance, with a value of 1 representing a perfect fit. Values near or below 0 imply that the model does not adequately capture the data's underlying patterns.

Collectively, these metrics provide a comprehensive performance evaluation by simultaneously assessing absolute prediction errors, quantified by MSE and MAE, and relative predictive capability measured by the R². This combination ensures a robust and well-rounded assessment of the corrosion rate prediction models.

2.6. SHAP-based feature selection

SHAP is a model-agnostic interpretability framework grounded in cooperative game theory, providing a theoretically rigorous and consistent mechanism for feature attribution in machine learning predictions. In this approach, each input feature is regarded as an independent participant in a coalition game, and the model output is considered the payoff of the coalition. The SHAP value of a given feature is computed as the average of its marginal contributions across all possible subsets of features. This formulation ensures that the feature importance measure is comparable and fair across different model types, while effectively capturing nonlinear interactions among variables. Consequently, SHAP is particularly advantageous in applications requiring robust and physically meaningful feature importance analysis.[43-45]

To identify the most influential input variables and improve model robustness, this study adopts SHAP to evaluate the global importance of each feature. SHAP values were used as a tool to rank input features according to their relative contribution to model prediction.

For a given feature X_k, its SHAP value represents the marginal contribution to the model output, averaged over all possible subsets of features. This is mathematically defined as shown in Eq. (13):

$$\varphi_k = \sum\left[|S|! \times \frac{(M-|S|-1)!}{|M|!}\right] \times [f(S \cup \{X_k\}) - f(S)] \tag{13}$$

where $f(S)$ denotes the model prediction based on a subset S of features, and M is the total number of input features.

To assess the global importance of each feature across the dataset, the mean absolute SHAP value is computed by averaging the absolute SHAP values across all N samples, as shown in Eq. (14):

$$\bar{\varphi}_k = \frac{1}{N}\sum_{i=1}^{N}\left|\varphi_k^{(i)}\right| \tag{14}$$

where $\varphi_k^{(i)}$ is the SHAP value of feature X_k for the i-th sample. Features with larger $\bar{\varphi}_k$ values are considered more relevant to the model's predictive process.

In this paper, SHAP is utilized solely as a feature selection tool, where only features with high global importance are retained. This enables the elimination of redundant or weakly informative inputs, leading to a more compact and efficient model without compromising prediction accuracy.

3. Results and discussion

3.1 Model benchmarking and selection

To systematically identify the most suitable ML models for predicting atmospheric corrosion rates, eight representative algorithms were *systematically benchmarked* in this paper. These models span four learning paradigms: linear models, kernel-based regressors, ensemble methods, and deep learning architectures. As illustrated in Fig. 2, the proposed corrosion prediction framework integrates data preprocessing, model training, hyperparameter optimization, and performance evaluation, enabling a comprehensive and standardized comparison across all candidate models. The models evaluated include Ridge Regression, Lasso Regression, SVR, Decision Tree, Random Forest, Gradient Boosting, XGBoost, and Neural Network (NN).[46-50] These methods are widely adopted in materials informatics and have shown strong potential in modeling complex relationships within high-dimensional datasets.

All models were trained on a unified dataset comprising alloy compositions, environmental parameters, and exposure times. To ensure a fair and unbiased comparison, each model underwent independent hyperparameter optimization before training. Specifically, Ridge Regression, Lasso Regression, and Decision Tree models, which are characterized by relatively low-dimensional hyperparameter space, were optimized using exhaustive grid search over manually defined parameter ranges, with five-fold cross-validation employed to select the configuration minimizing the average validation error. In contrast, for models with higher-dimensional and more complex hyperparameter spaces, including Random Forest, Gradient Boosting, XGBoost, and NN, Bayesian optimization was adopted to efficiently explore the search space. This approach leverages a probabilistic surrogate model in combination with the EI acquisition function to balance exploration of uncertain regions with exploitation of promising areas, thereby significantly reducing the number of required evaluations and ultimately enabling effective identification of the optimal hyperparameter configuration.

For clarity and reproducibility, the hyperparameters listed in Table 5 are defined as follows. In Ridge and Lasso regression, alpha denotes the regularization strength, with larger values imposing a stronger penalty on coefficient magnitude to mitigate overfitting. For tree-based models, max_depth specifies the maximum depth of the tree, thereby controlling model complexity, while n_estimators indicates the number of trees in ensemble methods such as Random Forest, Gradient Boosting, and XGBoost. The parameter random_state represents the seed for random number generation to ensure consistent results across repeated runs. In Gradient Boosting, XGBoost, and NN models, learning_rate determines the step size for updating model parameters, where smaller values generally improve generalization but require more iterations. For SVR, kernel defines the type of kernel function; in this study, the radial basis function (rbf) kernel was employed to map input features into a higher-dimensional space, enabling the capture of nonlinear relationships. In NN training, epochs refer to the total number of complete passes through the training dataset, and batch_size specifies the number of samples processed before each parameter update.

The final hyperparameter settings determined for each model are listed in Table 5. These optimized configurations, including learning rates, regularization parameters, tree depths, and training epochs, were used for subsequent model training and performance evaluation.

After optimization, all models were trained using their respective best-performing hyperparameters and evaluated via five-fold cross-validation to assess generalization capability. The predictive results are summarized in Table 6 and compared visually in Fig. 3 using three metrics: R^2, MAE, and MSE. As shown in Table 6, the two linear models, Ridge

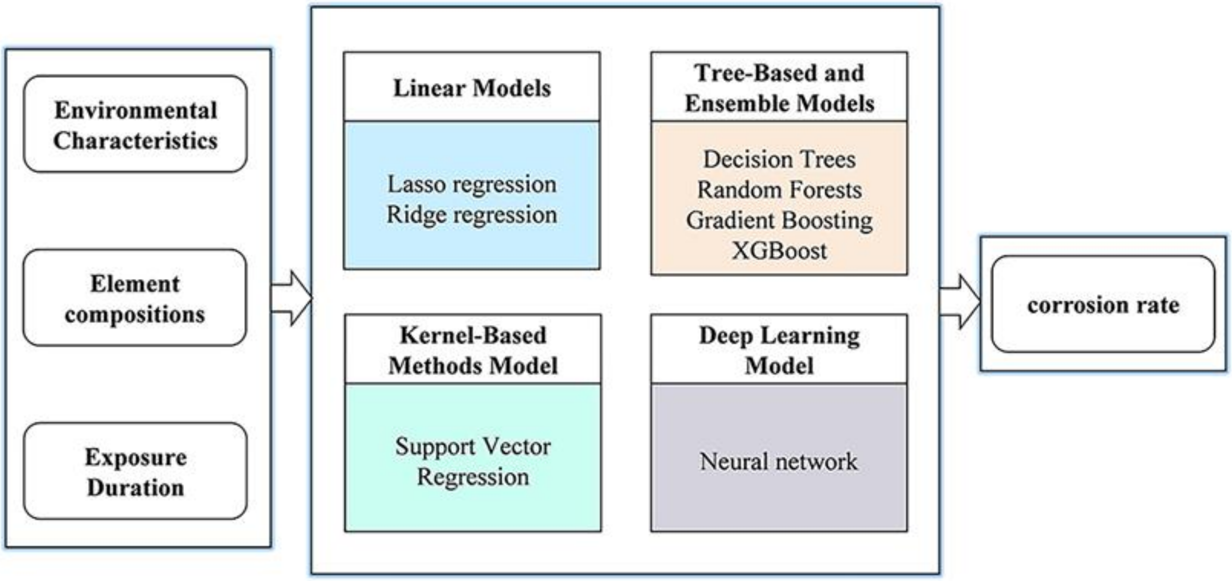

Fig. 2: Schematic illustration of the corrosion rate prediction framework using eight representative ML models.

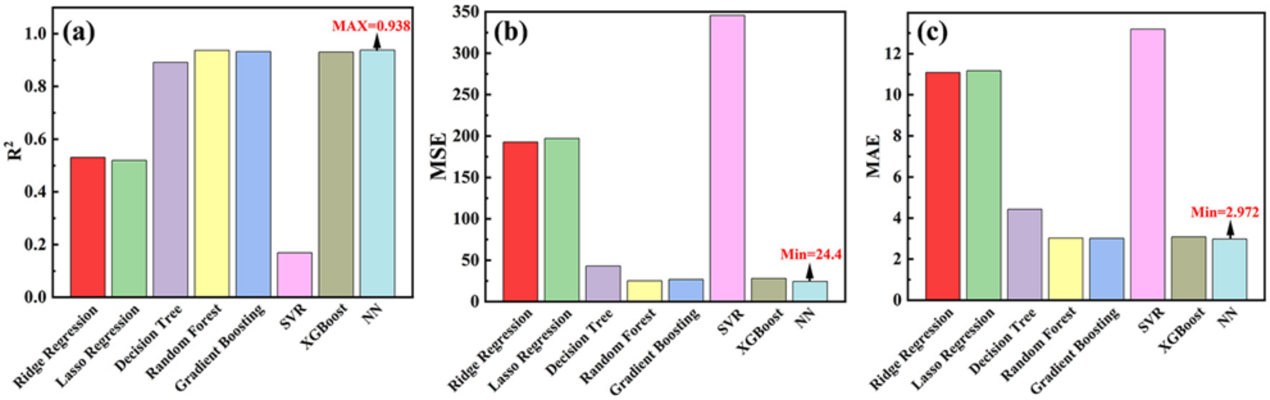

Fig. 3: Model performance comparison based on R², MAE, and MSE.

Table 5: Results of hyperparameter optimization for each ML algorithm.

Model	Hyperparameter	Optimized Value
Ridge Regression	alpha	1.0
Lasso Regression	alpha	0.1
Decision Tree	max_depth	5
Random Forest	n_estimators	100
	random_state	42
Gradient Boosting	learning_rate	0.1
	n_estimators	100
	max_depth	3
XGBoost	n_estimators	100
	learning_rate	0.1
	max_depth	3
SVR	kernel	rbf
NN	epochs	1500
	batch_size	64
	learning_rate	0.0003

Regression and Lasso Regression, exhibited limited performance, with R² values of 0.531 and 0.519 and MAE values exceeding 11. These results suggest that linear models fail to capture the nonlinear feature interactions that are often intrinsic to atmospheric corrosion phenomena.

SVR performs even worse, with an R² of only 0.169 and the highest error values among all models. This poor performance is attributed to the kernel function's limited capacity to model noisy or high-variance data without extensive tuning. In contrast, the tree-based ensemble models show significantly improved results: Decision Tree achieves an R² of 0.891, while Random Forest, Gradient Boosting, and XGBoost deliver R² scores of 0.937, 0.932, and 0.930, respectively. These ensemble methods benefit from model averaging and residual learning, which help reduce overfitting and enhance robustness.

Notably, the baseline NN outperforms all other models across all three evaluation metrics, achieving the highest R² value of 0.938, the lowest MAE of 2.972, and the smallest MSE of 24.400. These results confirm the NN's superior capacity in modeling complex, multi-factorial relationships that govern atmospheric corrosion. Fig. 3 highlights this performance advantage, establishing the NN as the most accurate and generalizable model among those evaluated in this benchmarking task.

3.2 SHAP-based feature selection and analysis

To enhance input relevance and reduce model complexity, a SHAP-based feature selection strategy was applied to the previously optimized NN model. The network architecture and training hyperparameters were deliberately held constant to ensure that any observed changes in model performance were solely attributable to modifications in the input feature set.

SHAP values were calculated to quantify the marginal contribution of each input variable to the predicted corrosion rate. Compared with conventional feature selection approaches such as permutation importance or recursive feature elimination, SHAP offers a model-agnostic and mathematically grounded mechanism derived from cooperative game theory. This allows for consistent and fine-grained assessment of feature importance, particularly suitable

Table 6: Performance comparison of ML models for corrosion rate prediction.

Model	MAE	MSE	R²
Ridge Regression	11.085	192.729	0.531
Lasso Regression	11.167	196.972	0.519
Decision Tree	4.428	43.040	0.891
Random Forest	3.021	25.289	0.937
Gradient Boosting	3.003	26.811	0.932
SVR	13.190	345.625	0.169
XGBoost	3.077	27.896	0.930
NN	2.972	24.400	0.938

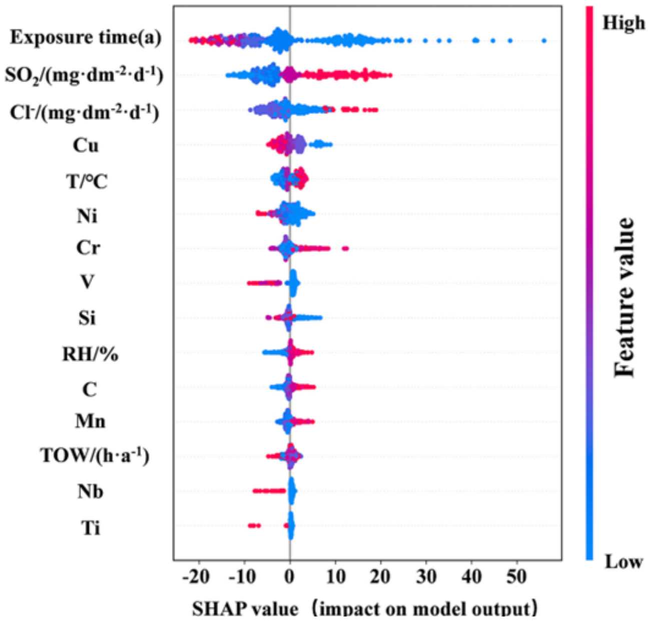

Fig. 4: SHAP beeswarm plot of feature impact.

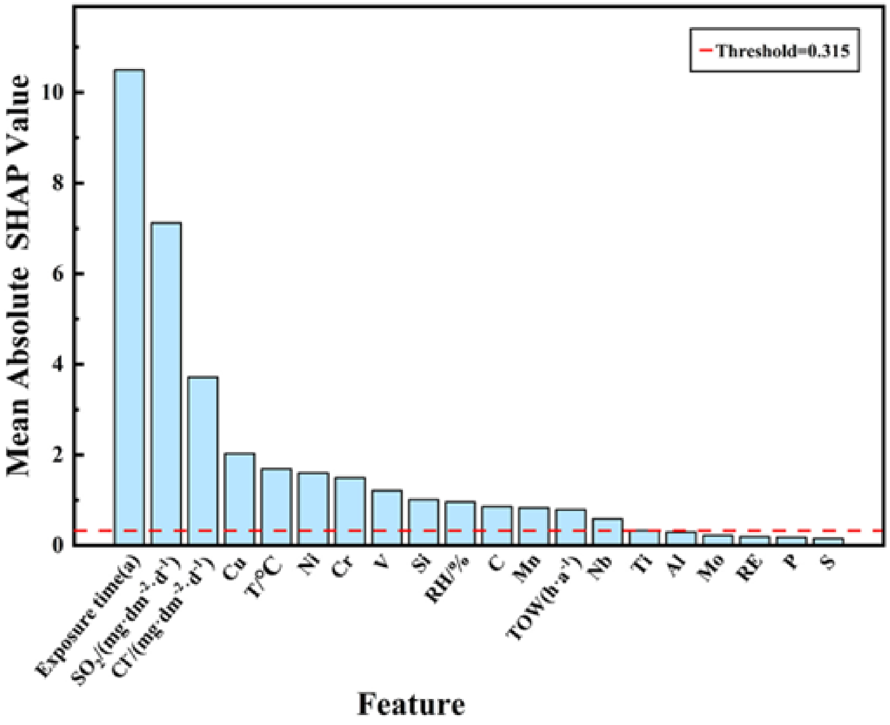

Fig. 5: Mean absolute SHAP values of key features.

for capturing nonlinear relationships among environmental and compositional variables.

To visualize the contribution of each feature across the entire dataset, a SHAP beeswarm plot was generated, as shown in Fig. 4. In this plot, each point corresponds to an individual sample. The x-axis represents the SHAP value, indicating the impact of the feature on the predicted corrosion rate. The color gradient reflects the original feature value, where red corresponds to higher values and blue to lower values. Features are arranged in descending order of their mean absolute SHAP values, providing a clear representation of both feature importance and the dependency between feature values and model outputs.

Subsequently, the mean absolute SHAP values for all features were aggregated and ranked, as illustrated in Fig. 5. Among the 20 original input features, only a subset showed substantial contributions to model output. In particular, Exposure time(a), SO_2 deposition rate, Cl^- deposition rate, and Cu content emerged as the most influential variables. These features align with well-established physical mechanisms in atmospheric corrosion, such as the roles of acidic pollutants, halide ions, and alloying elements in accelerating corrosion kinetics.

To eliminate redundant or weakly informative features, a pruning threshold was applied: input variables with a mean absolute SHAP value less than 3% of the maximum were excluded from the training set. This threshold selection was based on prior empirical studies and domain knowledge, which suggest that features with negligible attribution may introduce noise and degrade the generalization capability of the model. The red dashed line in Fig. 5 indicates this pruning threshold, which ultimately reduced the dimensionality of the input space from 20 to 15 features.

Based on the retained high-contribution features, the NN was retrained using the reduced input set, while maintaining the original network architecture and training parameters. This updated model is referred to as the ENN, which incorporates both structural optimization and data-driven feature selection.

3.3. Model evaluation and comparative analysis

To systematically evaluate the predictive performance and generalizability of the models after feature selection, all candidate algorithms were retrained using the reduced input set. This step aims to assess whether the retained features are sufficient to support accurate predictions across different learning paradigms, while also examining each model's sensitivity to input dimensionality. The updated performance metrics, including MAE, MSE, and R^2, are summarized in Table 7, and the comparative results before and after feature selection are illustrated in Fig. 6.

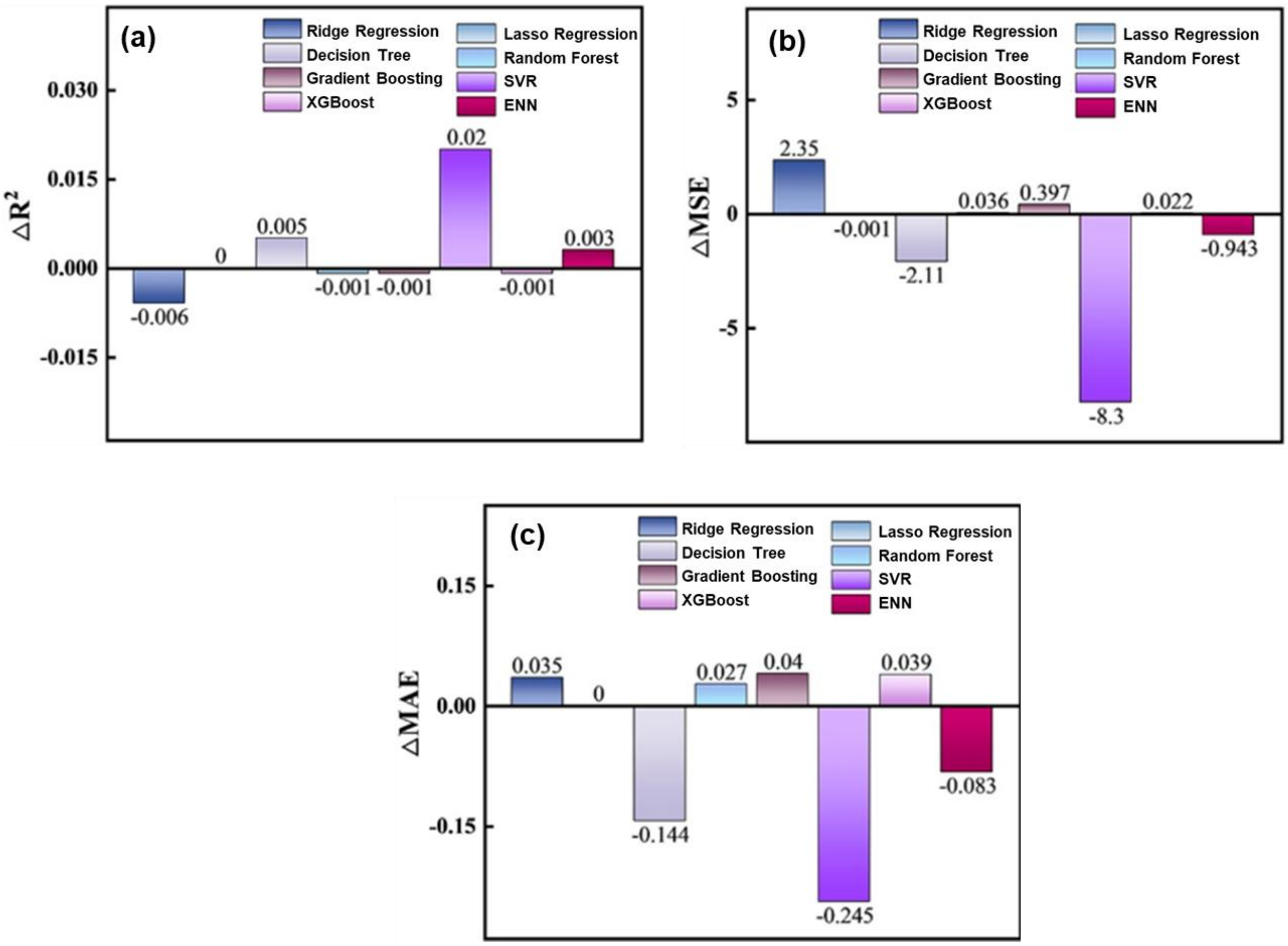

Fig. 6: Comparison of model performance metrics before and after feature selection. (a) ΔR^2; (b) ΔMSE; (c) ΔMAE.

Table 7: Performance comparison of ML models for corrosion rate prediction after feature selection.

Model	MAE	MSE	R²
Ridge Regression	11.120	195.077	0.525
Lasso Regression	11.167	196.971	0.519
Decision Tree	4.284	40.930	0.896
Random Forest	3.048	25.325	0.936
Gradient Boosting	3.043	27.208	0.931
SVR	12.945	337.330	0.189
XGBoost	3.116	27.918	0.929
ENN	2.889	23.457	0.941

Table 8: Environmental categories and characteristics according to ISO 9224.

Corrosion Category	Corrosivity Level	Typical Environmental Characteristics
C3	Medium	Urban; light industrial; mild coastal
C4	High	Industrial, moderate coastal
C5	Very High	Heavy industrial, high-salinity coastal

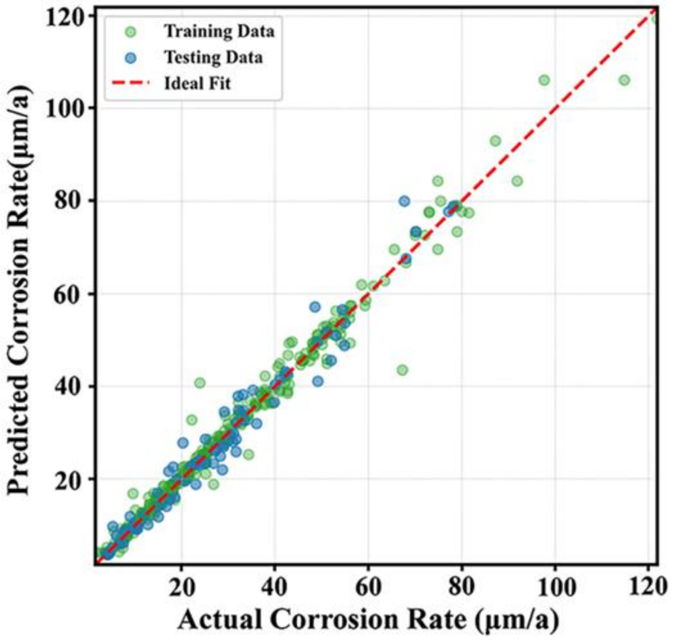

Fig. 7: Actual vs. predicted corrosion rates using the ENN model on training and testing sets.

Among all models, the ENN exhibited the most notable improvement. With only physically meaningful and high-contribution features retained, the ENN achieved an MAE of 2.889, an MSE of 23.457, and an R² of 0.941. These values represent relative improvements of 2.79% in MAE and 3.87% in MSE compared to the baseline NN model. This demonstrates that the NN, characterized by high nonlinear modeling capability, benefits considerably from input dimensionality reduction, resulting in enhanced generalization and reduced risk of overfitting.

Ensemble methods such as Decision Tree, Random Forest, Gradient Boosting, and XGBoost also maintained strong performance after feature selection, with slight improvements in some cases. For instance, the R² of the Decision Tree increased from 0.891 to 0.896, and Random Forest preserved its high R² of 0.936 with slightly reduced error metrics. These results highlight the robustness of ensemble models to feature redundancy, attributable to mechanisms such as feature subsampling and residual learning, which inherently mitigate the impact of irrelevant inputs.

In contrast, linear models like Ridge Regression and Lasso, as well as kernel-based methods like SVR, showed limited or no improvement. SVR remained the poorest performer with an R^2 of only 0.189, suggesting that such models are less responsive to feature refinement when facing highly nonlinear or noisy data. This reinforces the importance of aligning model complexity with the structural characteristics of the data.

As shown in Fig. 6, the ENN's performance gains are visually evident across all three metrics, clearly distinguishing it from the other models. To further validate its predictive capability, Fig. 7 presents the actual versus predicted corrosion rates on both training and testing sets. The results show a strong alignment along the diagonal, indicating that the ENN captures the underlying corrosion patterns effectively and performs well on held-out validation samples.

To evaluate the effectiveness and applicability of the proposed ENN model, a two-fold validation strategy was implemented, focusing on both short-term prediction accuracy and the model's capability to reproduce realistic long-term corrosion evolution under various environmental conditions.

The model was first validated using one-year corrosion data of WP720 steel obtained from Taiyuan, where the 1-year data point was held out as the validation set. As shown in Fig. 8, the predicted corrosion rate was 17.25 μm/a, closely matching the measured value of 16.86 μm/a. The resulting absolute error was 0.39 μm/a, corresponding to a relative error of only 2.31%. This strong agreement demonstrates that the ENN model maintains high numerical accuracy when applied to practical environments not included in training.

3.4 Model validation and long-term trend assessment

In addition to pointwise verification, we conducted field exposure experiments in Taiyuan and obtained corrosion rate data for WP720 steel at multiple exposure durations. As illustrated in Fig. 9, the measured corrosion rate exhibited a typical time-evolving pattern: a sharp initial decline followed by gradual stabilization. This trend is consistent with the known corrosion behavior of weathering steels, in which a dense rust layer forms during early exposure and inhibits

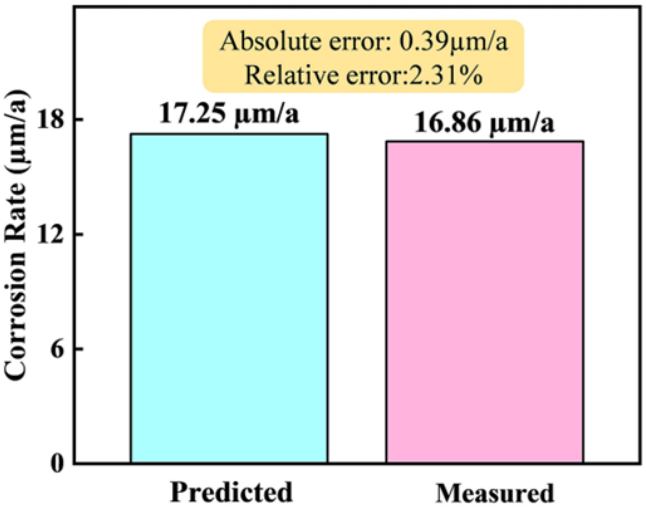

Fig. 8: Comparison of actual and predicted corrosion rates for WP720 steel.

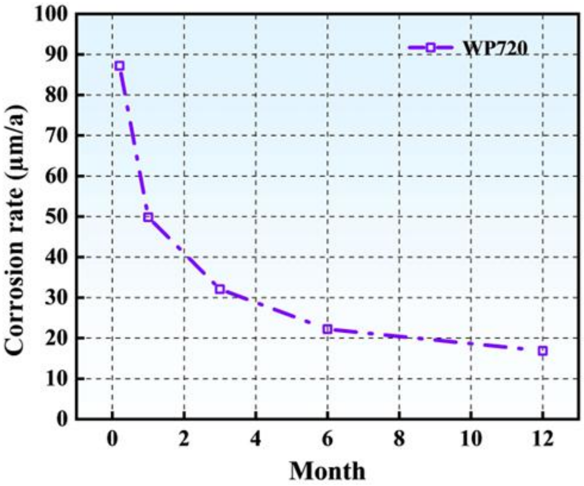

Fig. 9: Measured corrosion rates of WP720 steel over exposure time.

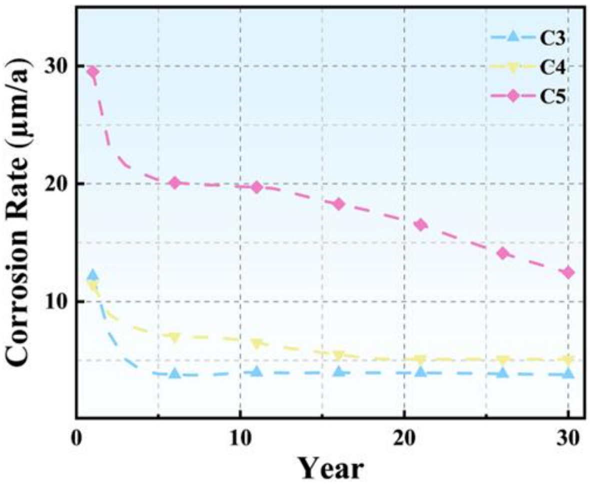

Fig. 10: Predicted corrosion rates over 30 years for WP720 steel under C3, C4, and C5 atmospheric environments.

further degradation. The experimentally obtained trend provides a practical reference for assessing the model's ability to capture time-dependent corrosion characteristics.

To further assess the model's long-term predictive capability, we simulated corrosion behavior over 30 years under three atmospheric categories defined by ISO 9224: C3, C4, and C5, corresponding to medium, high, and very high corrosivity levels, respectively. These categories are associated with typical urban and light industrial conditions, industrial and coastal environments, and marine or heavy industrial atmospheres. The specific environmental parameters for each category are summarized in Table 8. Based on these inputs, the ENN model generated corrosion profiles as illustrated in Fig. 10.

Across all three categories, the predicted corrosion rates exhibited a steep decline in early years and gradually plateaued with time. Notably, the predicted trends in Fig. 10 closely resemble the field-observed kinetics shown in Fig. 9, which further reinforces the model's ability to capture realistic corrosion evolution across time. The smooth transition of corrosion behavior across environmental severities demonstrates the robustness, reliability, and physical consistency of the ENN model.

In summary, the proposed model exhibits excellent predictive performance over both short-term and long-term timescales, and across diverse atmospheric conditions. These results highlight its strong potential for practical deployment in atmospheric corrosion monitoring and service life prediction of weathering steel structures.

4. Conclusion

This paper developed a predictive model for estimating the atmospheric corrosion rate of weathering steel. The main conclusions are as follows:

Among eight benchmark ML models, the NN demonstrated the best performance after hyperparameter tuning via grid search and Bayesian optimization, achieving an R^2 of 0.938.

Based on SHAP feature importance analysis, an ENN was developed, resulting in improved prediction accuracy with a coefficient of determination of 0.941.

The ENN model was validated through one-year independent field data (relative error: 2.31%) and long-term predictions under ISO 9224-defined environments, confirming its reliability and practical applicability.

Future work will focus on expanding the dataset to cover more weathering steel types and environmental conditions, leveraging transfer learning to improve generalizability, and integrating the model into digital twin frameworks for practical corrosion monitoring and service life assessment.

Acknowledgments

The authors gratefully acknowledge the Key Scientific Research Project of Shanxi Province (Grant No. 202302050201015) and the National Natural Science Foundation of China (Grant No. 52401103).

Conflict of Interest

There is no conflict of interest.

Supporting Information

Not applicable.

CRediT Statement

Yan Bai: Conceptualization, Methodology, Investigation; Formal analysis, Data curation, Visualization, Writing – Original draft, Writing – Review & editing. **Baosheng Liu:** Supervision, Project administration, Funding acquisition, Writing – Review & editing. **Yuezhong Zhang:** Investigation, Methodology, Validation, Resources. **Shaohua Zhang:** Investigation, Data curation, Validation. **Pengpeng Wu:** Software, Formal analysis, Visualization. **Xiaoxia Ren:** Resources, Supervision, Writing – Review & editing. **Yinghui Wei:** Supervision, Project administration, Funding acquisition.

References

[1] Y. Wu, Y. Wang, Y. Hu, F. Liu, G. Che, Y. Li, Effects of different photovoltaic installation modes on soil bacterial community structure, diversity, and assembly mechanisms in rocky desertification areas, *Engineered Science*, 2025, **35**, 1506, doi: 10.30919/es1506.

[2] J. Liu, X. Shen, Global PV supply Chains: Costs and energy savings, GHG emissions reductions, *Energy Policy*, 2025, **205**, 114716, doi: 10.1016/j.enpol.2025.114716.

[3] S. Rana, N. Vandewetering, J. Powell, J. Á. Ariza, J. M. Pearce, Geographical dependence of open hardware optimization: case study of solar photovoltaic racking, *Technologies*, 2023, **11**, 62, doi: 10.3390/technologies11020062.

[4] K. Jain, V. Agarwal, S. S. Ahmad, S. Mohapatra, P. K. Srivastava, P. B M, R. Bhat, Multi-parametric optimization of wired electrical discharge machining process to minimize damage cause in steel - a soft computing based taguchi-grey relation analysis approach, *Engineered Science*, 2022, **20**, 267-274, doi: 10.30919/es8e729.

[5] D. Thierry, D. Persson, G. Luckeneder, K.-H. Stellnberger, Atmospheric corrosion of ZnAlMg coated steel during long term atmospheric weathering at different worldwide exposure sites, *Corrosion Science*, 2019, **148**, 338-354, doi: 10.1016/j.corsci.2018.12.033.

[6] T. Gu, Y. Liu, C. Peng, P. Zhang, Z. Wang, Initial atmospheric corrosion of zinc-aluminum-magnesium coated steel and galvanized steel in regions of extremely cold and industrial climate, *Materials Chemistry and Physics*, 2022, **291**, 126686, doi: 10.1016/j.matchemphys.2022.126686.

[7] T. Chen, T. Shang, G. Jiang, H. Teng, W. Liu, X. He, X. Zhou, W. Liu, X. Cheng, X. Li, C. Liu, Effect of SO_2 and NH_3 on the corrosion failure of Zn-Al-Mg coatings, *Surface and Coatings Technology*, 2024, **493**, 131244, doi: 10.1016/j.surfcoat.2024.131244.

[8] Y. Xu, L. Yu, Y. Chen, Y. Tian, C. Liu, J. Wang, G. Liu, Y. Bai, C. Guo, J. Liu, P. Zhang, Evaluation of the anticorrosion properties of passivation solution containing different metal ions coated on a steel surface, *Engineered Science*, 2023, **24**, 917, doi: 10.30919/es917.

[9] Y. Xu, Y. Zhang, Y. Shu, H. Song, X. Shu, Y. Ma, L. Hao, X. Zhang, X. Ren, Z. Wang, X. Zhang, Composition and leaching toxicity of hydrochloric acid pickling sludge generated from the hot-dip galvanized steel industry, *ACS Omega*, 2022, **7**, 13826-13840, doi: 10.1021/acsomega.2c00121.

[10] H. Kihira, M. Kimura, Advancements of weathering steel technologies in Japan, *Corrosion*, 2011, **67**, 95002-95002-13, doi: 10.5006/1.3628684.

[11] C. Han, Z. Li, X. Yang, J. Wang, Corrosion behavior and mechanical performance of weathering steel in industrial and rural atmospheric environments, *Construction and Building Materials*, 2024, **411**, 134284, doi: 10.1016/j.conbuildmat.2023.134284.

[12] T. Wierzbicki, G. Rutkowska, M. Żółtowski, M. Nagirniak, Behavior of weathering steel in artificial harsh environment, *Materials*, 2024, **17**, 5919, doi: 10.3390/ma17235919.

[13] Y. Tang, Y. Guo, P. Ji, B. Li, C. Xia, S. Zhang, J. Zhang, X. Zhang, R. Liu, Optimizing the corrosion performance of rust layers: role of Al and Mn in lightweight weathering steel, *NPJ Materials Degradation*, 2024, **8**, 32, doi: 10.1038/s41529-024-00450-0.

[14] C. Han, Q. Yu, S. Wang, M. Qiao, Q. Wang, Research on the influence of Mo on the corrosion mechanism of 1%Ni weathering steel in simulated marine atmospheric environments, *Metals*, 2025, **15**, 430, doi: 10.3390/met15040430.

[15] Su Zexing, Li Menglin, Li Liren, Liu Chengzhi, Cheng Shengwei, Liu Xifeng, Kang Jianguang, Li Taotao, Temperature and deformation distribution during hot continuous rolling process of WP720 super weathering resistant steel, *Journal of Netshape Forming Engineering*, 2025, **17**, 89-95, doi: 10.3969/j.issn.1674-6457.2025.07.010.

[16] R. Bender, D. Féron, D. Mills, S. Ritter, R. Bäßler, D. Bettge, I. De Graeve, A. Dugstad, S. Grassini, T. Hack, M. Halama, E.-H. Han, T. Harder, G. Hinds, J. Kittel, R. Krieg, C. Leygraf, L. Martinelli, A. Mol, D. Neff, J.-O. Nilsson, I. Odnevall, S. Paterson, S. Paul, T. Prošek, M. Raupach, R. I. Revilla, F. Ropital, H. Schweigart, E. Szala, H. Terryn, J. Tidblad, S. Virtanen, P. Volovitch, D. Watkinson, M. Wilms, G. Winning, M. Zheludkevich, Corrosion challenges towards a sustainable society, *Materials and Corrosion*, 2022, **73**, 1730-1751, doi: 10.1002/maco.202213140.

[17] M. Rajendran, D. Subbian, Deep learning in corrosion assessment and control: a critical review of techniques and challenges, *Corrosion Reviews*, 2025, doi: 10.1515/corrrev-2024-0060

[18] T. Best, V. J. Gelling, An industrial perspective on challenges in the lifetime prediction of organic coatings: a century retrospective review, *Corrosion*, 2023, **79**, 304-327, doi: 10.5006/4180.

[19] Z. Dong, L. Ding, Z. Meng, K. Xu, Y. Mao, X. Chen, H. Ye, A. Poursaee, Machine learning-based corrosion rate prediction of steel embedded in soil, *Scientific Reports*, 2024, **14**, 18194, doi: 10.1038/s41598-024-68562-w.

[20] Z. He, M. Yang, L. Wang, E. Bao, H. Zhang, Concentrated photovoltaic thermoelectric hybrid system: an experimental and machine learning study, *Engineered Science*, 2021, **15**, 47-56, doi: 10.30919/es8d440.

[21] N. Mohan, S. A. Kalam, R. Mahaveerkannan, M. Shah, J. S. Yadav, M. U. Jaipur, V. Sharma, M. U. Jaipur, P. S. Naik, S. Paramashivaiah, C. E. College, Statistical evaluation of machining parameters in drilling of glass laminate aluminum reinforced epoxy composites using machine learning model, *Engineered Science*, 2022, **20**, 244-251, doi: 10.30919/es8e716.

[22] S. Bunian, M. A. Al-Ebrahim, A. A. Nour, Role and applications of artificial intelligence and machine learning in manufacturing engineering: a review, *Engineered Science*, 2024, 29, 1088, doi: 10.30919/es1088.

[23] Y. Zhi, Z. Jin, L. Lu, T. Yang, D. Zhou, Z. Pei, D. Wu, D. Fu, D. Zhang, X. Li, Improving atmospheric corrosion prediction through key environmental factor identification by random forest-based model, *Corrosion Science*, 2021, **178**, 109084, doi:

10.1016/j.corsci.2020.109084.

[24] W. Jin, Z. Chen, W. Liu, Q. Quan, Z. Ren, Establishment of an improved Elman neural network model for predicting the corrosion rate of 3C steel in marine environment and analysis of the factors affecting model accuracy, *Metals*, 2025, **15**, 27, doi: 10.3390/met15010027.

[25] P. Wang, H. Wu, X. Liu, C. Xu, Machine learning-assisted prediction of stress corrosion crack growth rate in stainless steel, *Crystals*, 2024, **14**, 846, doi: 10.3390/cryst14100846.

[26] N.-L. Tran, T.-H. Nguyen, V.-T. Phan, D.-D. Nguyen, A machine learning-based model for predicting atmospheric corrosion rate of carbon steel, *Advances in Materials Science and Engineering*, 2021, **2021**, 6967550, doi: 10.1155/2021/6967550.

[27] Y. Zhi, T. Yang, D. Fu, An improved deep forest model for forecast the outdoor atmospheric corrosion rate of low-alloy steels, *Journal of Materials Science & Technology*, 2020, **49**, 202-210, doi: 10.1016/j.jmst.2020.01.044.

[28] L. Yan, Y. Diao, Z. Lang, K. Gao, Corrosion rate prediction and influencing factors evaluation of low-alloy steels in marine atmosphere using machine learning approach, *Science and Technology of Advanced Materials*, 2020, **21**, 359-370, doi: 10.1080/14686996.2020.1746196.

[29] H. Wan, S. Liu, D. Song, W. Cai, Y. Wang, L. Geng, C. Chen, Prediction of industrial atmospheric corrosion and evaluation of influencing factors based on machine learning, *Journal of Materials Engineering and Performance*, 2025, **34**, 24589-24599, doi: 10.1007/s11665-025-11201-w.

[30] Y. Song, Q. Wang, X. Zhang, L. Dong, S. Bai, D. Zeng, Z. Zhang, H. Zhang, Y. Xi, Interpretable machine learning for maximum corrosion depth and influence factor analysis, *NPJ Materials Degradation*, 2023, **7**, 9, doi: 10.1038/s41529-023-00324-x.

[31] National Material Corrosion and Protection Data Center, China Environmental Corrosion Information Platform, accessed October 10, 2024, http://www.ecorr.org.cn/.

[32] H. Cano, I. Díaz, D. de la Fuente, B. Chico, M. Morcillo, Effect of Cu, Cr and Ni alloying elements on mechanical properties and atmospheric corrosion resistance of weathering steels in marine atmospheres of different aggressivities, *Materials and Corrosion*, 2018, **69**, 8-19, doi: 10.1002/maco.201709656.

[33] B. Daneshian, D. Höche, O. Ø. Knudsen, A. W. B. Skilbred, Effect of climatic parameters on marine atmospheric corrosion: correlation analysis of on-site sensors data, *NPJ Materials Degradation*, 2023, **7**, 10, doi: 10.1038/s41529-023-00329-6.

[34] S. Feliu, M. Morcillo, S. Feliu Jr, The prediction of atmospheric corrosion from meteorological and pollution parameters: I. Annual corrosion, *Corrosion Science*, 1993, **34**, 403-414, doi: 10.1016/0010-938x(93)90112-t.

[35] S. Feliu, M. Morcillo, S. Feliu Jr, The prediction of atmospheric corrosion from meteorological and pollution parameters: II. Long-term forecasts, *Corrosion Science*, 1993, **34**, 415-422, doi: 10.1016/0010-938x(93)90113-u.

[36] H. P. Vinutha, B. Poornima, B. M. Sagar, Detection of outliers using interquartile range technique from intrusion dataset, *Information and Decision Sciences*, Springer, Singapore, 2018, 511-518, doi: 10.1007/978-981-10-7563-6_53.

[37] E. Acuña, C. Rodriguez, The treatment of missing values and its effect on classifier accuracy, *Classification, Clustering, and Data Mining Applications*, Springer, Berlin, Heidelberg, 2004, 639-647, doi: 10.1007/978-3-642-17103-1_60.

[38] ISO 8407:2009, Corrosion of metals and alloys-Removal of corrosion products from corrosion test specimens, International Organization for Standardization, Geneva, 2009.

[39] ISO 9226:2012, Corrosion of metals and alloys-Corrosivity of atmospheres-Determination of corrosion rate of standard specimens for the evaluation of corrosivity, International Organization for Standardization, Geneva, 2012.

[40] B. Bischl, M. Binder, M. Lang, T. Pielok, J. Richter, S. Coors, J. Thomas, T. Ullmann, M. Becker, A.-L. Boulesteix, D. Deng, M. Lindauer, Hyperparameter optimization: Foundations, algorithms, best practices, and open challenges, *WIREs Data Mining and Knowledge Discovery*, 2023, **13**, e1484, doi: 10.1002/widm.1484.

[41] J. Snoek, H. Larochelle, R. P. Adams, Practical Bayesian optimization of machine learning algorithms, *Advances in Neural Information Processing Systems (NIPS)*, 2012, **4**, 2951–2959.

[42] A. K. Maurya, S. Tiwari, A. G. Bhavani, N. Park, N. G. S. Reddy, Artificial neural network-based modeling of atmospheric zinc corrosion rates using meteorological and pollutant data, *Coatings*, 2025, **15**, 538, doi: 10.3390/coatings15050538.

[43] E. Kalita, H. El Aouifi, A. Kukkar, S. Hussain, T. Ali, S. Gaftandzhieva, LSTM-SHAP based academic performance prediction for disabled learners in virtual learning environments: a statistical analysis approach, *Social Network Analysis and Mining*, 2025, **15**, 65, doi: 10.1007/s13278-025-01484-1.

[44] E. Kalita, S. S. Oyelere, S. Gaftandzhieva, K. N. V. P. S. Rajesh, S. K. Jagatheesaperumal, A. Mohamed, Y. M. Elbarawy, A. S. Desuky, S. Hussain, M. A. Cifci, P. Theodorou, S. Hilčenko, J. Hazarika, T. Ali, Educational data mining: a 10-year review, *Discover Computing*, 2025, **28**, 81, doi: 10.1007/s10791-025-09589-z.

[45] J. Xiong, S.-Q. Shi, T.-Y. Zhang, Machine learning of phases and mechanical properties in complex concentrated alloys, *Journal of Materials Science & Technology*, 2021, **87**, 133-142, doi: 10.1016/j.jmst.2021.01.054.

[46] C. Pei, Q. Ma, J. Zhang, L. Yu, H. Li, Q. Gao, J. Xiong, A novel model to predict oxidation behavior of superalloys based on machine learning, *Journal of Materials Science & Technology*, 2025, **235**, 232-243, doi: 10.1016/j.jmst.2025.01.071.

[47] R. Ramprasad, R. Batra, G. Pilania, A. Mannodi-Kanakkithodi, C. Kim, Machine learning in materials informatics: recent applications and prospects, *NPJ Computational Materials*, 2017, **3**, 54, doi: 10.1038/s41524-017-0056-5.

[48] Y. Zhou, J. Liu, K. Chen, H. Shi, X. Shang, Z. Que, Z. Shen, L. Zhang, X. Zeng, Predicting intergranular stress corrosion cracking of stainless steels in high-temperature water by incorporating crystallographic factor, *Acta Materialia*, 2025, **297**, 121322, doi: 10.1016/j.actamat.2025.121322.

[49] S. Dong, J. Xiong, Y. Tian, S. Chen, L. Wei, T.-Y. Zhang, Design of corrosion-resistant eutectic high-entropy alloys *via* hybrid data-driven and expert-guided strategies, *Corrosion*

Science, 2025, **253**, 113024, doi: 10.1016/j.corsci.2025.113024.

[50] L. Wu, Y. Xiao, M. Ghosh, Q. Zhou, Q. Hao, Machine learning prediction for bandgaps of inorganic materials, *ES Materials & Manufacturing*, 2020, **9**, 34-39, doi: 10.30919/esmm5f756.

Publisher's Note: Engineered Science Publisher remains neutral with regard to jurisdictional claims in published maps and institutional affiliations.